Automated correction of spin-history related motion artefacts in fMRI

Muresan, L; Renken, R.; Roerdink, J.B.T.M.; Duifhuis, H.

Published in:
Ieee transactions on biomedical engineering

DOI:
10.1109/TBME.2005.851484

Publication date:
2005

Automated Correction of Spin-History Related Motion Artefacts in fMRI: Simulated and Phantom Data

Lucian Muresan[(a,c)], Remco Renken[(b,c)], Jos B.T.M. Roerdink[(a,c)], *Senior Member, IEEE*
and Hendrikus Duifhuis[(b,c)], *Member, IEEE,*

***Abstract*— This paper concerns the problem of correcting spin-history artefacts in fMRI data. We focus on the influence of through-plane motion on the history of magnetization. A change in object position will disrupt the tissue's steady-state magnetization. The disruption will propagate to the next few acquired volumes until a new steady state is reached. In this paper we present a simulation of spin-history effects, experimental data, and an automatic two-step algorithm for detecting and correcting spin-history artefacts. The algorithm determines the steady-state distribution of all voxels in a given slice and indicates which voxels need a spin-history correction. The spin-history correction is meant to be applied before standard realignment procedures.**

In order to obtain experimental data a special phantom and an MRI compatible motion system were designed. The effect of motion on spin-history is presented for data obtained using this phantom inside a 1.5 T MRI scanner. We show that the presented algorithm is capable of detecting the occurrence of a displacement, and it determines which voxels need a spin-history correction. The results of the phantom study show good agreement with the simulations.

***Index Terms*— Functional magnetic resonance imaging, spin-history, automated motion artefact correction, spin-history simulator, movable MRI-phantom.**

I. Introduction

Functional magnetic resonance imaging (fMRI) is used to identify brain areas involved in executing a specific task. The identification is based on the Blood Oxygen Level Dependent (BOLD) effect [1]–[3]. Upon activation, blood oxygenation levels change locally in the brain, generating 1-5% signal changes at the most common magnetic field strength (1.5 T). Any signal modulation not related to the BOLD effect can be interpreted as additional noise in fMRI [4]–[6]. Thus, other processes which induce changes of the same order of magnitude or more, can compromise the final statistical analysis. One such process is the effect of motion on the signal intensity via spin history. The reason is that the fMRI signal is a function of both the current position and the spin excitation history, which depends on the object's position during all previous scans. A displacement during the experiment can modify the intensity of the subsequently scanned volumes, even if those volumes are not displaced themselves. As we will see below, spin-history artefacts will occur especially in those voxels whose relaxation time T_1 is much larger than the repetition time T_R. The relative change of signal intensity due to this spin-history modulation can range from 3-7%, depending on the presence of gaps between the slice profiles. In our view, the treatment of spin-history effects in the fMRI literature has left various open questions. We formulate those questions and propose possible answers.

A description of the impact of noise on the interpretation of fMRI data can be found in Parrish et al. [4]. These authors describe a method that allows the qualitative and quantitative comparison of fMRI methods based on the signal-to-noise ratio (SNR). An experimental study of different sources of noise in fMRI can be found in Zarahn *et al.* [5], and Aguirre *et al.* [6]. Head motion is one of the main sources of noise in fMRI. Depending on (1) the time at which the change in head position occurs, (2) the pulse sequence used, (3) the type of motion, (4) the amplitude of motion, and (5) the interpolation scheme used for realignment, different motion correction algorithms have been proposed. The majority of these techniques uses retrospective motion correction. That is, time series data are processed after all data have been acquired [7]–[10]. Another technique, known as prospective acquisition correction, updates pulse sequence parameters based on the previously acquired volumes. In this way, influences of through-plane motion on the history of magnetization is minimized [11]–[13]. The retrospective and prospective methods only correct for motion that occurs *between* the acquisition of volumes. If a change in position occurs *during* acquisition of a volume, e.g. between acquisition of individual slices, a realignment of the slice stacks can be used to correct for the motion [14]. Finally, motion during the acquisition of Fourier data of a single slice is assumed to be negligible when using fast imaging techniques such as echo-planar imaging (EPI).

In this paper we restrict ourselves to head motion during the interval between two successive volume acquisitions, which is the most common type of head motion in fMRI. The primary effect of the movement is a change of head position in the scanner reference system. There are several mechanisms that influence the magnetic state of the scanned object through changes in position. The first mechanism is via the main B_0 magnetic field irregularities. In order to counter these effects, shimming is performed, but only once, i.e. prior to each measurement, although in principle each new position would require a new shimming. These susceptibility-induced artefacts are difficult to correct. A second mechanism is via the geometry of excitation profiles. Because the excitation profiles are not homogeneous across the object, motion will cause a different impact of these profiles on the magnetic state of the system. If the spin system has no time to return to equilibrium before the next excitation pulse occurs, the magnetic state of the system will depend on the history of past magnetic states. This motion-related effect is known as spin history. The spin-history problem was formulated by Friston *et al.* [9]. They proposed to reduce the intensity changes by regressing the data against the movement time series derived from the registration procedure. The third mechanism is that motion-related effects, not related to the magnetic properties of the object, are generated by interpolation procedures used for realignment [15].

We focus on the following questions: (1) does the set of parameters used for acquiring the data result in a spin-history artefact? (2) in which voxels can an intensity modulation generated by spin-history be expected? (3) how can we automatically detect spin-history artefacts? and (4) how can we correct spin-history artefacts? To answer these questions we developed a spin-history simulator program to better understand the link between object motion and spin history. Furthermore, we designed a physical phantom with a user-definable T_1-map, together with a computer controlled, MRI compatible, motion system to study spin-history artefacts generated by through-plane motion. Also, an algorithm to correct spin-history artefacts was developed. Data from the simulation program and the

The authors are with (a) Institute for Mathematics and Computing Science, (b) Biomedical Engineering and the (c) Institute for Behavioral and Cognitive Neurosciences (BCN), University of Groningen, P. O. Box 800, 9700 AV Groningen, The Netherlands. E-mail: roe@cs.rug.nl

movable phantom were used to check the correction algorithm.

Our spin-history correction algorithm is a two-step procedure, which can be summarized as follows. Step 1 is the detection phase. First, we use the (usually discarded) first few scans after initialization to classify all voxels into three types: (i) Equilibrium voxels, whose relaxation is so fast that they can be regarded as being in equilibrium; (ii) Steady-State voxels, with a high T_1-value relative to the repetition time, which enter into a steady state far from equilibrium; (iii) Null voxels, with an intensity too small to be considered for further analysis. Then, during data acquisition, the equilibrium voxels are used as 'motion-only' detectors and the steady-state voxels as 'motion plus spin-history' detectors, so that we can detect, prior to realignment, voxels where motion or spin-history modulation occurred. Step 2 of the procedure is the actual correction which makes proper intensity changes of the affected voxels.

Another approach for correcting spin-history artefacts we initially considered is to first estimate maps of the relaxation time T_1 and equilibrium magnetization $M_{\rm eq}$, then use exact information about repetition time, flip angles and slice profile, and finally recalculate, using the Bloch equations [16], the intensity value of the voxel at a given location and time. Although this approach might work for simulated data, we have found that for real data the estimation of T_1 just from the fMRI series does not give reliable values.

The remainder of this paper is organized as follows. In section II we present a simulation of translational object motion, where data acquisition is carried out following the usual protocol in fMRI, but not yet taking brain activation into account. This allows us to estimate the magnitude and location of these artefacts, and also propose an algorithm to correct them. In section III we describe an experimental setup of a specifically designed MRI phantom, which can be moved under computer control with high accuracy inside the scanner, and which can validate the spin-history correction algorithm on data obtained by scanning this phantom. Finally, in section IV we present the overall conclusions and implications for future work.

II. Simulations and correction algorithm

A. Description of the mechanism

In fMRI, pulse sequences are usually designed under the assumption that the scanner reference system and the object reference system have the same relative position during the entire measurement. The spin history depends on the slice profile (flip angle profile) in the object reference system. Each RF pulse has a corresponding spatial map $\alpha(x, y, z)$ of flip angles in the scanner reference system. In the object reference system this map will rotate or translate if the scanned object is rotated or translated. Thus a change in position of the scanned object influences the spin history via the flip angle profile. Most motion correction algorithms that focus on the alignment of the slice stacks [14] do not take this spin-history effect into account.

If there is motion between acquisition of two successive volumes, then the spin history is affected by the position history. If all the regions of the object were in magnetic equilibrium prior to each volume acquisition, there would be no spin-history effect. However, because the spins are excited periodically and relatively rapidly, they do not return to equilibrium, but reach a certain (non-equilibrium) steady state [17]. Normally, the first few (dummy) scans are discarded from further analysis because they contain a very intense spin-history modulation. The steady state of the scanned object is maintained as long as the temporal periodicity of the RF excitations and gradients is maintained in the object reference system. A change in position relative to the slice profiles will destroy this pattern. Thus a transition period towards a new steady state will occur. The transient state can last for several volume acquisitions after a displacement. The intensity of the signal in those volumes will change during this transition. In the next section we present a quantitative analysis of the spin-history mechanism.

TABLE I
Summary of notations.

Orientation of the Oz-axis:	along B_0
Small volume under consideration:	dV
Initial longitudinal magnetization of dV:	$M_z(0) = M_{\rm eq}$
Total number of RF pulses:	N
Flip angle maps:	$(\alpha_1(\vec{r}) \ldots, \alpha_N(\vec{r}))$
Times at which RF pulses occur:	$t_1, \ldots, t_N$
Corresponding positions of dV:	$\vec{R}_1, \ldots, \vec{R}_N$

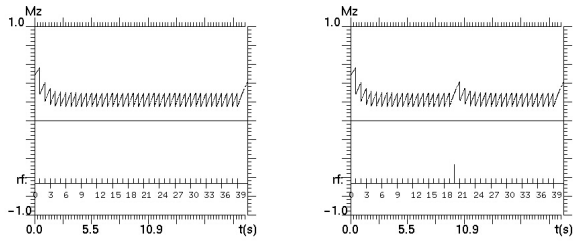

Fig. 1. Behavior of the longitudinal magnetization M_z of a small volume part dV when there were no changes in object position (left) and in the case when at the $20th$ RF pulse a 'back-and-forth' motion occurred (right). There is a temporary disruption of the steady state at initialization and following each motion, i.e. at pulse IDs 0 and 20.

B. Spin-history simulator

1) Model description: As mentioned before, the spin history of a scanned object is influenced by a number of factors, such as: (1) position and shape of the slice excitation profiles, (2) the times at which RF pulses occur, (3) the set of positions of the scanned object for each slice acquisition, and (4) maps of the equilibrium magnetization and relaxation time (that is, their spatial distribution). The simulation program calculates the behavior of the longitudinal magnetization M_z of a small part dV of the scanned object as a function of time. The two main parameters for this volume, dV, are the longitudinal relaxation time T_1 and the equilibrium magnetization $M_{\rm eq}$ in the static magnetic field B_0. Our notations and conventions are summarized in Table I. The flip angle for each position $\vec{r}$ in the scanner reference system is defined by the shape of the RF pulses, together with the applied strength of the slice selection gradient. The set of positions of the small volume dV defines the position history for dV. From the position of the entire rigid object it is possible to infer this set of positions for every small subvolume of the scanned object. The motion can have components both parallel and perpendicular to the longitudinal axis Oz.

For the simulation we make the following assumptions: (1) The acquisition of one slice is based on one RF pulse. The time interval between successive RF pulses is constant. (2) RF pulses are treated as instantaneous, i.e. their duration is negligible compared to other relevant time scales (T_1, repetition time). (3) The change in object position occurs between acquisitions of two successive volumes. That is, possible motion *during* the acquisition of one slice is neglected. (4) The intensity of the acquired image is proportional to the transversal component M_{xy} of the magnetization immediately after the RF pulse. (5) Other effects that could result from a displacement are neglected, such as shimming effects, interpolation errors, susceptibility effects and non-uniformity of B_0.

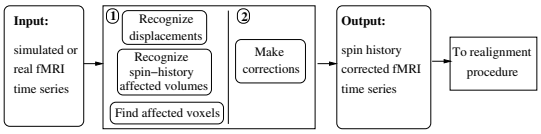

Fig. 2. Diagram of the correction algorithm. The input is the raw (not realigned) fMRI time series. The algorithm detects (phase 1) and corrects (phase 2) the affected volumes. The output is the corrected time series which can be subject to realignment or other post-processing.

2) Recapitulation of theoretical background: The impact of the k^{th} RF pulse on the magnetization of dV will depend on the relative position of dV with respect to the excitation profile $\alpha_k(\vec{r})$. At t=0, dV is inside the scanner at position $\vec{R}_1$. The first RF pulse occurs at $t_1 = 0$ and will tilt the magnetization vector over a certain flip angle $\alpha_1(\vec{R}_1)$. The longitudinal magnetization $M_z(t)$ has discontinuities each time an RF pulse occurred, i.e. at times $t_1, t_2, \ldots, t_N$. We use the notation $M_z(t_k^-)$ and $M_z(t_k^+)$ for the value of $M_z(t)$ immediately before and after the k^{th} RF pulse, respectively. The longitudinal magnetization $M_z(t_1^-)$ immediately before the first RF pulse is defined as the equilibrium magnetization, i.e. $M_z(t_1^-) = M_{\rm eq}$.

Straightforward application of the Bloch equations [16] gives the following results for the longitudinal magnetizations:

$$M_z(t_k^-) = M_{\rm eq}(1 - e^{-\frac{t_k - t_{k-1}}{T_1}}) + M_z(t_{k-1}^+)\, e^{-\frac{t_k - t_{k-1}}{T_1}} \quad (1)$$

$$M_z(t_k^+) = M_z(t_k^-)\cos(\alpha_k) \quad (2)$$

$$M_z(t) = M_{\rm eq}(1 - e^{-\frac{t - t_k}{T_1}}) + M_z(t_k^+)\, e^{-\frac{t - t_k}{T_1}},\ t_k < t < t_{k+1} \quad (3)$$

Starting with magnetic equilibrium, application of a periodic RF sequence to dV will drive M_z towards a steady state (Fig. 1, left) during a transition period. A temporary change in object position will destroy the steady state, resulting in a transition (Fig. 1, right). The value M_z^∞ of the steady-state magnetization can be determined by letting k go to infinity in Eq. 1. Assuming a constant value α for the flip angles and a constant repetition time, (i.e. $t_{k+1} - t_k = T_R$), the result is [18]:

$$M_z^\infty = M_{\rm eq}\,\frac{1 - e^{-T_R/T_1}}{1 - \cos(\alpha)\, e^{-T_R/T_1}}. \quad (4)$$

There are two limiting cases, depending on whether the value of T_1 is much smaller or larger than the repetition time, respectively:

$$M_z^\infty = M_{\rm eq} \qquad \text{if } T_1 \ll T_R \quad (5)$$

$$M_z^\infty = M_{\rm eq}\,\frac{T_R/T_1}{1 - \cos(\alpha)} \qquad \text{if } T_1 \gg T_R \quad (6)$$

3) Simulation parameters: In the simulations, two types of object displacement are applied: (1) a vertical displacement in one direction; and (2) a vertical displacement which is immediately followed by the reverse displacement. The types of displacement (1) and (2) will be denoted by 'out-of-plane' and 'back-and-forth', respectively. In future work, we will also consider the case of rotational motion.

The parameters we used to generate the fMRI time series and the displacements are given in Table II. Other important input parameters of the simulation program are: the 3D maps containing the spatial distribution of $M_{\rm eq}$ and T_1, and the position of the object along the z-direction (perpendicular to the slice orientation). The 3D maps were generated from intensity image files (PGM or analyze format).

C. Spin-history artefact detection algorithm

This subsection describes Step 1 of the correction procedure, i.e. the *detection* phase, during which we find voxels which were affected by pure motion, or by a motion plus spin-history modulation, respectively. The full spin-history artefact correction algorithm is summarized in Fig. 2. The input of this procedure is an fMRI time series, including the first few acquired volumes, prior to realignment. Displacements occur at unknown time points. We use the two types of displacement introduced in section II-B, i.e. 'out-of-plane' or 'back-and-forth'.

TABLE II

PARAMETERS USED TO GENERATE THE FMRI TIME SERIES. dZ IS THE DISTANCE BETWEEN THE GRID POINTS IN THE z-DIRECTION. THE NUMBER OF VOXELS IN A SLICE IS $n_x \times n_y$.

Displacement	Volume ID
1mm	14
2mm	19
-1mm	24
-2mm	34

Parameter	Value
Slice Width	2.6 mm
Gap	0.4 mm
Slice Profile	Rectangular
dZ	0.22 mm
nx, ny	79, 95
Repetition Time	1.7 s
Noise Percentage	3%
Flip Angle	60^o
#Pulses per volume	5
#Volumes	40

The output of the algorithm is: (1) a list of volume IDs where displacement occurred, (2) a list of volumes affected by spin-history, and (3) a list of voxels that need spin-history correction. On the basis of this output the artefact correction algorithm to be presented in section II-D will correct the intensity of affected voxels. We do not attempt to correct those volumes which were acquired at the very moment of displacement, because this involves a realignment procedure and is a subject well covered in the literature. To validate and test the robustness of the algorithm we used the realistic digital brain phantom [19], [20] to generate a realistic fMRI volume time series. White matter, grey matter and cerebrospinal fluid volumetric data sets are used to create a realistic spatial distribution of T_1 and $M_{\rm eq}$.

The detection algorithm consists of two phases. First, we use the first few (dummy) scans after initialization to classify all voxels into three distinct types. Then, during data acquisition, the different types of voxels can be used to determine, prior to realignment, where motion or spin-history modulation occurred. We now describe these two phases in more detail.

1) Voxel classification: We distinguish the following three classes of voxels:

- *Null voxels* [N-voxels]: Voxels with an intensity too small to be considered for further analysis. Such voxels occur for example in regions with no signal, i.e. the black area surrounding the scanned object[1].
- *Steady-state voxels* [SS-voxels]: Voxels with a high T_1-value relative to the repetition time, see Eq. 6, causing them to enter into a steady state far from equilibrium, cf. Fig. 3, left. The first few measured volumes will show a marked change of intensity.
- *Equilibrium voxels* [E-voxels]: Voxels with a small T_1 relaxation time compared to the repetition time, see Eq. 5, causing

[1]These voxels are important for detecting artefacts due to motion during k-space acquisition.

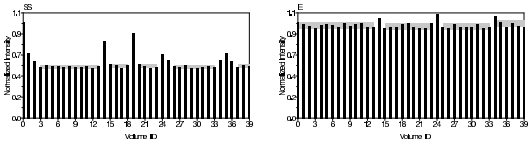

Fig. 3. Example of the behavior of intensity for 'back-and-forth' displacements. Left: an SS-voxel entering into a steady state far from equilibrium. Right: an E-voxel entering into a steady state close to equilibrium. Noise level in steady state is indicated in grey. There were four 'back-and-forth' displacements during the acquisition at volume IDs 14, 19, 24 and 34. For the SS-voxel (left) five steady states between the transient intervals can be observed.

them to quickly enter into a steady state close to equilibrium ('close' means within the noise level) between two successive excitations, cf. Fig. 3, right. A constant intensity (modulo noise fluctuations) after initialization will be observed.

This classification is needed when we want to discriminate between changes in intensities generated by displacement only (at the time instants when the actual change in position occurred), and those generated by spin history only (at time instants when no change in position occurred). The first few (3 or 4) volumes after initialization are used to create the classes of E-voxels and SS-voxels. If the intensity change in these first few volumes is of the same order of magnitude as the noise, we assume that we are dealing with an E-voxel type; otherwise, the voxel is classified as an SS-voxel. Although the property of being an E-voxel or SS-voxel depends on the T_1 relaxation time of voxels, the value of T_1 is not required to classify them. We only need to have access to the, usually discarded, first few volumes. An example is given in Fig. 3.

Null voxels are responsible for introducing bias to the steady-state distributions used in our spin-history detection and correction algorithm. These voxels have to be discarded by a proper choice of threshold for the voxel intensity. This threshold level is correlated to the noise in regions where there is no MR signal. A common threshold level is 10% of the maximum possible voxel intensity. The algorithm is not very sensitive to this parameter, because there are enough voxels in a transient state to make a robust decision about the times of displacement.

By using the E-voxels as 'motion-only' detectors and the SS-voxels as 'motion plus spin-history' detectors, we can detect, prior to realignment, where motion or spin-history modulation occurred. In addition, the E-voxels can be used to discriminate between 'out-of-plane' and 'back-and-forth' displacements.

2) Steady-state distribution: Our approach to detect displaced volumes and volumes affected by spin history is based upon the steady-state distribution of voxel intensities. This distribution is a statistical detector of the presence of motion and spin-history effects in a time series. For computational efficiency, we obtain the desired distribution by averaging over voxels within a single slice (excluding those with small intensity) instead of a complete volume. Of course, if a correction turns out to be required, this has to be applied to the whole volume (see section II-D).

To decide whether a voxel is in steady state at a given time t_k, we compare its intensity $I(t_k)$ with that at the previous time t_{k-1} and next time t_{k+1}. The voxel is classified as being in steady state if

$$|I(t_k) - I(t_{k+1})| < \Delta I_{\rm thr} \quad \text{or} \quad |I(t_k) - I(t_{k-1})| < \Delta I_{\rm thr}, \quad (7)$$

where $\Delta I_{\rm thr}$ is a threshold related to the noise level of the MRI scanner. In words, if the difference between the current intensity and either the previous or the next intensity is below the threshold, then the voxel is regarded as being in steady state (for $k = 0$ or $k = N$ only a single neighboring intensity is used). To illustrate this rule consider Fig. 3, right. According to Eq. 7, the E-voxel is in steady state at volume ID 13 and 15, separated by a non-steady state at ID 14.

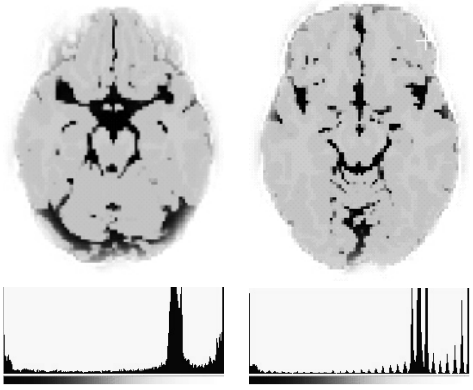

Fig. 4. Top row: T_1 maps for slice 0 (left) and slice 2 (right) of the digital brain phantom. Black represents high T_1 value, white represents low T_1 value. Bottom row: the corresponding image histograms.

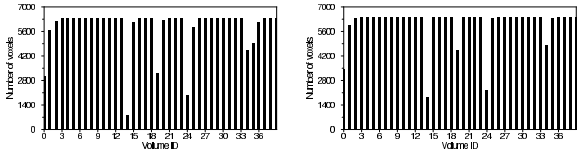

Fig. 5. Example of a steady-state distribution for slice 0 (left) and slice 2 (right), for a 'back-and-forth' displacement with both E-voxels and SS-voxels included. For each volume ID we plot the number of voxels which are in steady state. At first only E-voxels are in steady state. In the 3rd volume all voxels have reached steady state. The four displacements (at volume ID 14, 19, 24 and 34, respectively) destroy the steady state and so the number of voxels in steady state drops significantly.

3) 'Back-and-forth' displacement: Using Eq. 7, we can compute steady-state distributions of voxel intensities. First consider a 'back-and-forth' displacement. As an example, we consider two slices of the brain phantom whose T_1 maps are shown in Fig. 4. For these slices, we plot in Fig. 5 the total number of voxels (both E-voxels and SS-voxels) that are in steady state in a given volume versus the volume ID.

Next, the distribution for the SS-voxels is plotted separately, see Fig. 6. We observe a marked intensity change immediately after the time of displacement (at volume ID 15, 20, 25, 35), followed by a slow recovery of the destroyed steady state. So the impact of a displacement on SS-voxels propagates to the next one, two or even three acquired volumes. The effect is strongest for slice 0, which contains many voxels with high T_1 value, cf. Fig. 4. In contrast, the intensity of E-voxels is affected only at the time of displacement, because E-voxels enter very quickly into steady state after a displacement, cf. Fig. 6. Thus, there is no spin-history effect for this type of voxel. To determine in a robust way when displacement occurred, we need to average the times of displacement over many individual voxels. These moments of displacement are inferred from the time behaviour of the steady-state distribution. To this end, we compute the number of E-voxels in steady state in a complete slice. (Remember that the classification into E-voxels and SS-voxels has been made at initialization.) As is evident from the plots for the E-voxels, this steady-state distribution enables us to identify the volume IDs at which a displacement occurred.

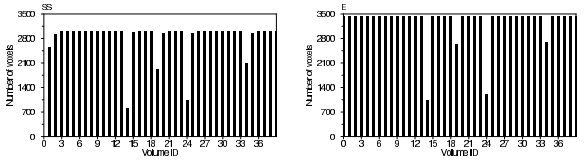

Fig. 6. Steady-state distribution for SS-voxels (left) and E-voxels (right), in slice 2, for a 'back-and-forth' displacement. In the case of SS-voxels the effect of motion propagates after each displacement (at volume ID 14, 19, 24, 34) to the subsequent (not displaced) volumes (15, 20, 25, 35, 36).

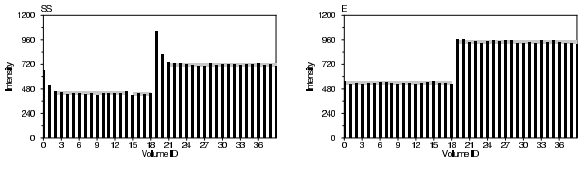

Fig. 7. Behavior of intensity in the case of an 'out-of-plane' displacement for an SS-voxel (left) and for an E-voxel (right). The E-voxel is in the next steady state right from the time (ID 19) when the displacement occurred. This feature is specific to 'out-of-plane' displacement.

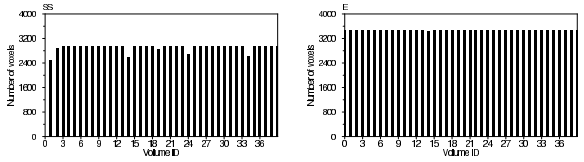

Fig. 8. Steady-state distribution in slice slice 2 for SS-voxels (left), and for E-voxels (right) for an 'out-of-plane' displacement. The four displacements occurred at volume ID 14, 19, 24 and 34, respectively.

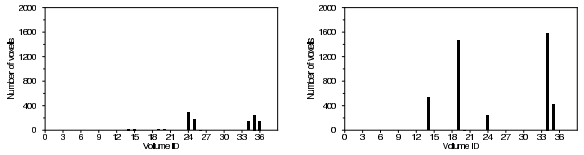

Fig. 9. Modified steady-state distributions of E-voxels for a 'back-and-forth' displacement (left) and an 'out-of-plane' displacement (right). The four displacements occurred at volume ID 14, 19, 24 and 34, respectively. The graph shows, for each volume ID k, the number of voxels which show a transition between two distinct steady-states precisely at time t_k.

4) 'Out-of-plane' displacement: Next we deal with the case of an 'out-of-plane' displacement, which is a change in position which lasts a number of time steps at least equal to the number of time steps needed for all voxels to reach a new steady state. In the example of Fig. 7, right, there is an initial steady state up to ID 18, followed by a new steady state starting at ID 19 (there are no 'non-steady states' for this voxel, in contrast to the case of a 'back-and-forth' displacement, cf. Fig. 3). This is explained by the fact that an E-voxel immediately reaches a new equilibrium steady state, so the displaced volume with ID 19 is already in steady state for this type of voxel. As a consequence, the corresponding steady-state distribution is almost flat, cf. Fig. 8, and does not allow robust determination of the times of displacement.

To detect 'out-of-plane' displacements we compute a modified steady-state distribution by counting at each time t_k those E-voxels which undergo a transition between two distinct steady-states precisely at time t_k, that is, the intensities $I(t_k)$ and $I(t_{k+1})$ should differ by an amount larger than the threshold $\Delta I_{\rm thr}$. A plot of the distribution of E-voxels having this property singles out the times when an 'out-of-plane' displacement occurred, cf. Fig. 9, right. For comparison, we also plotted in the same figure the same distribution for a 'back-and-forth' displacement. Clearly, this distribution is less appropriate to detect the 'back-and-forth' displacements. In this case, the transition between two different steady states is less sudden than in the case of 'out-of-plane' displacements, which shows up as broadened peaks in Fig. 9, left.

5) Automatic threshold selection: Calculation of the steady state for each voxel requires estimation of the noise in regions where there is no motion or spin-history disturbance. We used the following procedure to determine the corresponding noise threshold (see Eq. 7) automatically. Since, before applying the algorithm, we do not know exactly when a motion or spin-history change occurred, the initial noise threshold is set to two percent of the initial intensity value. In our experience, this starting value gives satisfactory results. If two steady-state average values are within the noise level, we 'glue' them together and update the threshold by recalculating the steady states. In a few (3-5) loops we obtain a stable threshold value for each voxel. From the distribution of the detected number of steady states (Fig. 10), we conclude that the automated procedure for finding the individual steady states for each voxel works reliably. In Fig. 3, left, we show an example of a voxel with 4 displacements which generated four transitions and thus 5 steady states. Indeed, the distribution of the detected number of steady states has a maximum at 5, cf. Fig. 10. However, due to the presence of noise, there are also a number of voxels with 2, 3, 4 or 6 detected steady states (Fig. 10).

D. Spin-history artefact correction algorithm

Now we present the correction of spin-history artefacts in the volumes acquired after a displacement. We will calculate standard deviation (SD) for each voxel in a slice (disregarding null voxels) to observe the effectiveness of our correction algorithm. To be able to compare different voxels, we use the normalized standard deviation (NSD), defined as the ratio between the standard deviation and the temporal average intensity of a voxel. The distribution of the NSD of all voxels in a slice is a good measure of the effects of motion.

We present simulation results obtained from the phantom data described in the previous section. From the output of the artefact detection algorithm we know which voxels are affected by spin history and at what times these changes in intensity occurred. There are three types of possible voxel intensity changes: (i) changes in the first few volumes during transition to steady state, (ii) a change due to displacement only, and (iii) a change due to spin history only. Each of these changes has a different impact on the standard deviation of time courses of voxel intensities. The detection algorithm presented in the previous section automatically detects these types of changes. We can calculate standard deviations taking into account or excluding the first volumes, the volumes affected by displacement or the volumes affected by spin history.

The impact of volume exclusions can be seen in Fig. 11. The plots show results prior to any correction. In Fig. 11, left, we included the types of change (ii) and (iii) and excluded type (i). The presence of spin-history artefacts and (pre-realignment) motion disturbances has a clear impact on the width of the distribution. When we exclude all (i), (ii) and (iii) volume types the resulting distribution reflects the usual noise distribution, with no other effects added (Fig. 11, right). An fMRI series, fully corrected for motion and spin history, should have such a distribution. So, by including or excluding the affected volumes, it is possible to detect the presence of motion-related artefacts from the shape of the normalized noise distribution.

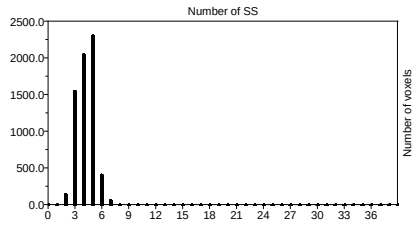

Fig. 10. Distribution of the detected number of steady states for individual voxels. There where 4 displacements, which should generate 5 steady states in an ideal noise-free case. Indeed, the distribution of the detected number of steady states has a maximum at 5. There were many voxels (especially those with small T_1) where the displacement had a small, below noise level, effect. This explains the massive presence of voxels with 3 and 4 steady states.

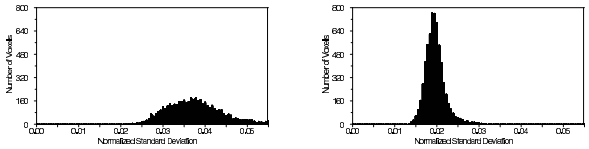

Fig. 11. Distributions of the normalized standard deviation, excluding voxels with low intensity. Exclusion classes are class (i): first 4 volumes; class (ii): displaced volumes (ID 14, 19, 24, 34); class (iii): spin-history affected volumes (ID 15, 19, 20, 25, 35, 36). Left distribution: excludes only class (i). Right distribution: excludes all three classes.

Spin-history artefacts become relevant when put in the framework of statistical analysis of fMRI data. The goal of fMRI analysis is to detect a very small change in intensity related to the task of the experiment, by applying statistical techniques to the time series. Any signal modulation not related to the BOLD effect is a confounding effect and can be interpreted as noise (in the sense of the General Linear Model used in the statistical analysis of fMRI data). Intensity fluctuations due to spin history occur in the volumes immediately following a displaced volume. Using the detection algorithm we can localize those affected volumes and the affected voxels in these volumes that are the source of this specific noise. The E-voxels, having a short T_1, do not introduce spin-history noise, but the SS-voxels do. The intensity in the transient regions (post-displacement volumes) often is different from the steady-state average value. The corrected value is the average intensity of the steady state closest in time to the instant of displacement. This correction is applied only to SS-voxels as identified by the spin-history detection algorithm.

The distribution of the standard deviation is a good global measure for the noise in the time series. Fig. 12 (left) shows this distribution before correction. After the correction (Fig. 12, right) the width of the distribution has decreased, and because we exclude the displaced volumes, the corrected distribution is similar to the noise distribution (Fig. 11, right). A very small amount of voxels has, after correction, a large normalized standard deviation (above 0.03). These voxels escaped detection and correction because the motion-related artefacts were below the automatic threshold used to detect motion-affected voxels. The distribution of the relative difference between the corrected value and the uncorrected value is given in Fig. 13. It clearly shows the presence of a significant amount of voxels that have a spin-history artefact in the range of 2 to 5 percent relevant for fMRI.

III. Experiments with a translating phantom

A. Phantom and MRI-compatible motion device

To apply precise translations at specific points in time, we designed a movable phantom which is computer controlled and MRI-compatible. The phantom consists of four major parts, see Fig. 14: the stage, the platform, the phantom body, and a computer with a pneumatic system to control the motion. The stage was custom made to fit into a Siemens head coil (Fig. 14). The stage also holds four pistons that are used to drive the platform, a guide rail or pivotal point, and four adjustment nuts that are used to restrict the motion of the platform. The platform has two possible degrees of motion: translation along the main axis of the bore and rotation around a vertical axis perpendicular to the main axis of the bore. Motion always occurs from a pre-set starting position to a pre-set end position. Maximal displacement and rotation are 2 cm and 10 degrees, respectively. Translation and rotation cannot be applied simultaneously.

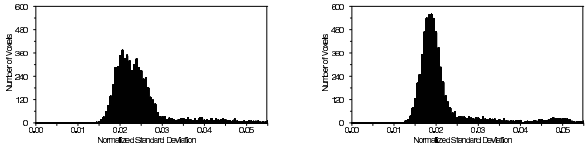

Fig. 12. Distribution of the normalized standard deviation before (*left*) and after (*right*) spin-history correction. Both distributions exclude null voxels. Excluded were the first 4 volumes and the displaced volumes (ID 14, 19, 24, 34).

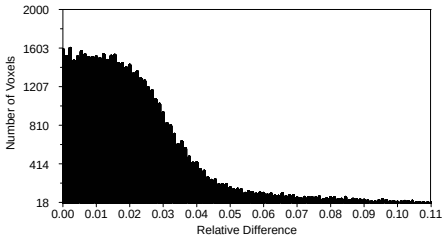

Fig. 13. Distribution of the relative difference between corrected and uncorrected voxel intensities.

On top of the platform different phantom bodies can be fixed. We have built a phantom body that allows us to spatially vary T_1 and T_2 properties. In this paper we concentrate on the T_1 dependence. The phantom body consisted of 5 layers; in each layer there are 169 cells in a square grid (13×13) pattern. Each cell had the dimensions of 5mm by 5mm by 10mm. The phantom was built from MRI neutral material, i.e. these materials gave no MR signal. The cells were filled with different solutions of copper sulphate (CuSO4) in water and sealed with a drop of kitchen oil. The T_1 property of the cells was varied by changing the concentration of copper sulphate [21], cf. Table III. The range of T_1 covers the possible T_1 values in human tissues. The T_1 values were determined by using an inversion recovery protocol with the following inversion recovery times: 600, 750, 1000, 1250, 1500, 2000, 3000, 4000, and 5000 ms. To the inversion recovery data intensity profiles an exponential function was fitted ($y(t) = 1 - 2\,e^{\frac{-t}{T_1}}$). The patterns we used are simple geometrical figures (Fig. 15). Motion of the phantom was controlled using a laptop computer equipped with Labview 6i (National Instruments). Through the serial port, the Labview program recorded the start of each slice acquisition via a trigger pulse generated by the MRI machine. These trigger pulses were used for the timing of the motion. Motion was controlled via two valves regulating the airflow to the pistons.

B. Experimental results

We performed several checks before the main EPI experiments. Anatomical high-resolution images (Fig. 15) were taken at each

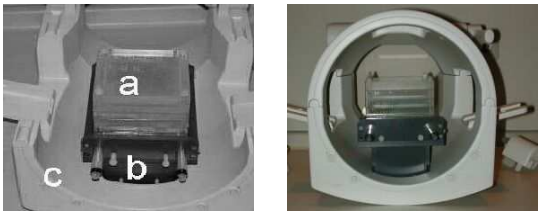

Fig. 14. Oblique view (left) and horizontal view (right) of the phantom (a) together with the motion device (b) inside the MRI head coil (c). Two pistons and two adjustment nuts are also visible.

TABLE III
THE SPATIAL T_1 DISTRIBUTION OF THE LAYERS OF THE PHANTOM.

Layer	Figure	T_1 (s) inside	T_1(s) outside
1	cross	0.9	0.1
2	triangle	1.0	0.9
3	cross	2.0	0.8
4	triangle	0.8	0.9
5	cross	0.1	0.8

position of the phantom. Using these images we were able to check displacement of the phantom. Measurements were made to check the spatial T_1 distribution (by inversion recovery and exponential fits, see Table III), the proper sealing of the cells and the absence of air bubbles.

In our experiments, we again used two types of object displacement: 'out-of-plane' and 'back-and-forth', as studied in section II. In the last experiment (9) the phantom was shaken back-and-forth from volume ID 9 to 18 and volume ID 29 to 38. In total, nine experiments were performed with parameters as shown in Table IV. The EPI measurements used the same pulse sequence and parameter values as in a normal fMRI experiment, cf. Table V. Each EPI measurement is characterized by three parameters which have the greatest impact on spin state: (1) the displacement of the phantom (2) the gap between slices and (3) the repetition time.

We looked for the relative changes in voxel intensity in the volumes measured after a displacement occurred. On the basis of the simulation results, we expect a propagation of the disturbance effect induced by the movement to these next volumes. This behavior was indeed found in the experimental data. For example, compare Fig. 16 with Fig. 3, where a very similar intensity profile is found after each 'back-and-forth' displacement.

Recall that a voxel is regarded as being in steady state, if the difference of the current intensity with either the previous or the next intensity is below a threshold determined by the noise level. In Fig. 17 we show the number of voxels which are in steady state for the slice 0 and slice 2. Null voxels were excluded. This figure can be compared to Fig. 5 which is obtained using the simulation program. Initially, only E-voxels are in steady state, corresponding to volume ID=0. After a transition time all voxels enter into steady state. At volume ID=19 a displacement occurs, so that the measured signal corresponds to different regions of the phantom (no realignment of the data was performed). As a result, the steady state is disrupted, so that the number of steady-state voxels in the next two volumes (IDs 20 and 21) is strongly reduced. At volume ID=22 all voxels are back in steady state.

The experimental results are in very good agreement with those of the simulation, cf. section II.

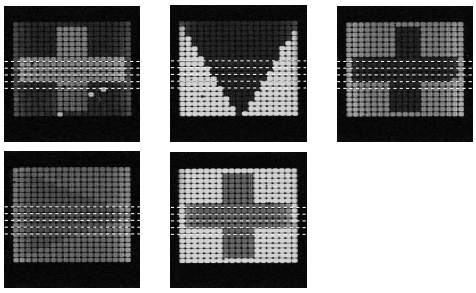

Fig. 15. High-resolution anatomical images of five different layers of the phantom. Slices acquired during MRI acquisition are perpendicular to the layers. Dashed white lines indicate the slice positions.

TABLE IV
PARAMETERS USED IN THE EXPERIMENTS. THE SLICE THICKNESS IS 5MM. 'DISPL.' INDICATES THE AMOUNT OF DISPLACEMENT, AND THE GAP FACTOR IS THE RATIO BETWEEN GAP AND SLICE WIDTH.

Exp. no.	Displ.	Gap Factor	Motion type at ID
1	7 mm	0.5	out-of-plane at 19
2	7 mm	0.5	back-and-forth at 19
3	7 mm	2	back-and-forth at 19
4	7 mm	2	out-of-plane at 19
5	2 mm	2	out-of-plane at 19
6	2 mm	2	back-and-forth at 19
7	2 mm	0.05	out-of-plane at 19
8	2 mm	0.05	back-and-forth at 19
9	2 mm	0.5	shake at 9-18 and 29-38

C. Spin-history correction of phantom data

Recall that the correction algorithm consists of two phases. First, there is automatic detection of displacements, and second, the actual intensity correction of affected voxels takes place (see also Fig. 2). In the nine experiments as listed in Table IV, we used different types and amounts of displacement, and different gap sizes. The distributions of NSD for slice 2, in experiments 2, 3, 6, and 8 (as listed in Table IV) are presented in Fig. 18.

The presence of spin-history artefacts can be observed by comparing the NSD distributions with and without spin-history affected volumes. When we exclude both displaced volumes and volumes affected by spin history (Fig. 18, left column) we get the expected distribution of NSD in the case of no motion. If we exclude only the displaced volumes, we do capture the spin-history artefacts (Fig. 18, right column). The first two rows (experiments 2 and 3) have a 7 mm displacement, so these two cases show larger effects compared to a 2 mm displacement (experiments 6 and 8, Fig. 18, last two rows). The experiment with the largest spin-history artefact was experiment 3, in which the gap size and the displacement were largest (Fig. 18, second row).

In the presence of a displacement, the presence of gaps between slices makes such slices behave similar to the first and last slice, which have an 'infinite' gap on one side. These boundary slices have a relatively large spin-history artefact, due to the fact that a displacement into the 'infinite' gap exposes the slice to an unsaturated region. Therefore, gap sizes should not be made too large. Obviously, there is a trade-off between increasing gap size to avoid overlap of successive slice profiles and decreasing gap size to avoid spin-history artefacts.

In the third experiment one 'back-and-forth' displacement occurred. This generates two steady states separated by a transient state due to displacement. Because of the presence of noise, the algorithm also detects voxels with one or three steady states (Fig. 19, left). The

TABLE V
PARAMETERS USED TO RECORD THE EPI IMAGES.

#slices per volume	5
#Volumes	40
Repetition Time	2 s
Echo Time	60 ms
Flip Angle	60^o
Scan Matrix	64×64
In Plane Resolution	3.44×3.44 mm

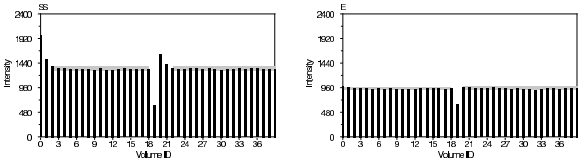

Fig. 16. Experiment 3: measurement results of the steady state destruction for two typical voxels in slice 2. An SS-voxel (left) enters in steady state after a transition phase. An E-voxel (right) recovers between two excitations. Motion at volume ID=19 destroys the steady state. The SS-voxel returns to steady state after two volumes (left), while the E-voxel recovers equilibrium immediately at the next volume ID=20 (right).

distribution of the duration of the steady states (that is, the number of scans in which the intensity remains constant, cf. Fig. 19, right) is related to the length of the transition phase at the beginning of the scan or after a displacement: the longer this transition phase, the shorter the steady states will last until the motion at fixed volume ID=19 occurs.

Recall from section II that E-voxels are used as detectors of displacement and type of displacement ('back-and-forth' or 'out-of-plane'). The algorithm uses the steady-state distribution for E-voxels to detect where a displacement occurred (Fig. 20, right). In all nine experiments, the detection algorithm successfully identified where the motion occurred and whether it was 'out-of-plane' or 'back-and-forth'. The steady-state distribution for SS-voxels (Fig. 20, left) contains information about both displacement and spin-history artefacts. From this distribution, the algorithm determines spin-history affected volumes. From Fig. 20, we see that the volume with ID=20 right after the displacement is affected, although it is itself undisplaced. The drop in the number of the voxels which are in steady state is more than 30% in Fig. 20, left, and about 50% in Fig. 20, right. This makes the detection algorithm very robust, even when using only part of the voxels of a single 64×64 slice.

As we mentioned in section II, the noise distribution of a spin-history corrected time series ideally should have the shape and position of the pure noise distribution. Therefore, the results of the correction algorithm are compared against the pure noise distribution of Fig. 21(a) as measured using the E-voxels. The NSD distribution before correction in Fig. 21(b) is very different from that shown in Fig. 21(a). After correction, cf. Fig. 21(c), the distribution is very close to that in Fig. 21(a). The spin-history artefact is largest in the third experiment, where also the largest values for displacement and gap were used (7 mm, gap factor of 2, see Table IV). At the other extreme is the 8th experiment (Fig. 18, last row) with 2 mm displacement and a gap factor of 0.05. In this experiment, the spin-history artefacts are very small as compared to the third experiment, and the noise distributions (Fig. 18, last row, left and right) are very similar.

The amount of steady-state disruption by a displacement is not a linear function of the amount of displacement or of the gap size. If, at the displaced position, a voxel happens to be in the middle of a gap, it will miss one or more excitations and will depart from

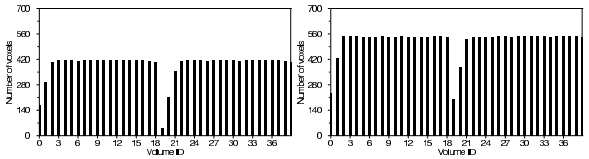

Fig. 17. Experiment 3: the measured time behaviour of the number of voxels in steady state, in slice 0 (left) and slice 2 (right).

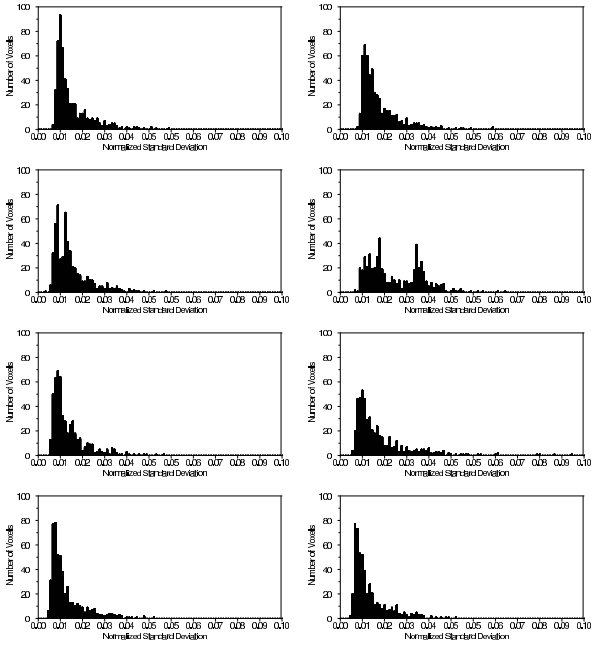

Fig. 18. Ratio between standard deviation and average intensity for the experiments 2, 3, 6 and 8 for slice 2. For the left column all (motion and spin-history) affected volumes were excluded. For the right column only the displaced volumes were excluded.

steady state. The disruption of the steady state will depend on the extent to which the displacement follows the spatial periodicity of the slice profiles. So it is not always true that bigger displacements imply a larger spin-history artefact. On the other hand, enlarging the gap between slices will increase the chance for spin-history artefacts to appear.

IV. SUMMARY AND CONCLUSIONS

We have studied spin-history artefacts in fMRI data. These can create spurious brain activations in fMRI studies and may influence realignment procedures. By correcting the spin-history artefacts, the power of the statistical analysis will increase [9], [22].

A two-step procedure for spin-history artefact correction was developed. In step 1, the (usually discarded) first few scans after initialization are used to classify all voxels as equilibrium, steady-state or null voxels, respectively, and during acquisition the different voxel types are used to detect voxels where the spin history disturbed the steady state. Step 2 is the actual correction procedure which makes proper intensity changes of the affected voxels. The proposed correction method is designed to be applied before the usual realignment procedures. The algorithm was validated using simulated and phantom data; both focused on through-plane translations of the object. In the simulations, data acquisition was carried out following the usual protocol in fMRI, but not yet taking brain activation into account.

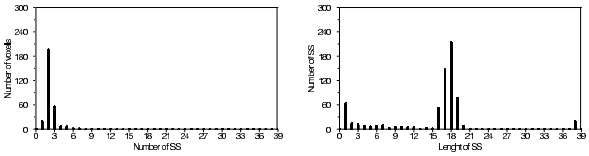

Fig. 19. Distribution of the number of steady states (left) and the duration of steady states (right) for slice 2 in experiment 3.

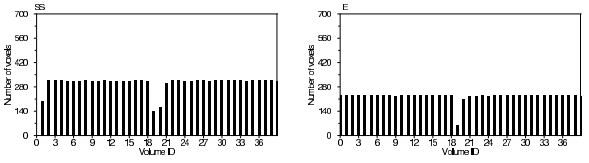

Fig. 20. Measured steady state distributions for SS-voxels (left) and E-voxels (right) for slice 2.

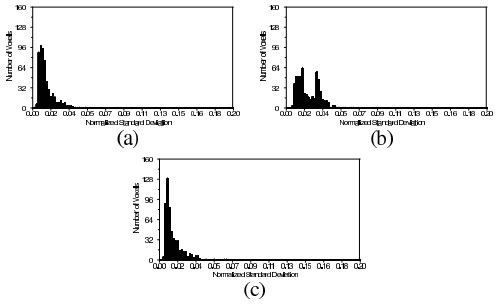

Fig. 21. Behavior of the correction algorithm in the third experiment. (a): normalized standard deviation (NSD) excluding both spin-history and motion affected volumes. (b, c): normalized standard deviation excluding displaced volumes before the correction (b) and after correction (c). Observe how the correction transforms the shape and position of the NSD distribution towards the pure noise distribution (a).

We showed that the proposed spin-history correction algorithm substantially decreases the noise induced by the spin-history artefact, and makes its distribution approach the pure noise distribution in the absence of motion. The experimental results confirmed the predictions made by the simulation program.

We plan to carry out a comparison of our algorithm with other procedures proposed in the literature which treat the spin-history noise influences as confounds. Future work will also deal with the validity of the correction algorithm in the presence of brain activation. We expect that in the latter case the analysis presented in this paper will remain essentially valid, in view of the fact that the time scale of the BOLD response is much larger than the time scale on which head motion occurs.

V. Acknowledgments

We gratefully acknowledge support from the Radiology Department of the Academic Hospital Groningen (AZG), and the School of Behavioral and Cognitive Neurosciences (BCN), the Netherlands. Special thanks are due to J.J. Land (technical workshop) and B.A. Pijpker (Dept. of Biomedical Engineering) for their help in constructing the phantom and motion system.

References

[1] S. Ogawa, T. M. Lee, A. S. Nayak, and P. Glynn, "Oxygenation sensitive contrast in magnetic resonance image of rodent brain at high magnetic fields", *Magn. Res. Med.*, vol. 14, pp. 68–78, 1990.

[2] S. Ogawa, D. Tank, R. Menon, J. Ellermann, S. Kimand H. Merkle, and K. Ugurbil, "Intrinsic signal changes accompanying sensory stimulation: functional brain mapping with magnetic resonance imaging", in *Proc. Natl. Acad. Sci. USA*, vol. 89, pp. 5951–5959, 1992.

[3] S. Ogawa, R. S. Menon, S. G. Kim, and K. Ugurbil, "On the characteristics of functional magnetic resonance imaging of the brain", *Annu. Rev. Biophys. Biomol. Struct.*, vol. 27, pp. 447–474, 1998.

[4] T. B. Parrish, D. R. Gitelman, K. S. LaBar, and M. M. Mesulam, "Impact of signal-to-noise on functional MRI", *Magn. Res. Med.*, vol. 44, pp. 925–932, 2000.

[5] E. Zarahn, G. K. Aguirre, and M. D'Esposito, "Empirical analyzes of BOLD fMRI statistics, I. spatially unsmoothed data collected under null-hypothesis conditions", *Neuroimage*, vol. 5, pp. 179–197, 1997.

[6] M. D'Esposito G. K. Aguirre, E. Zarahn, "Empirical analyzes of BOLD fMRI statistics, II. spatially unsmoothed data collected under null-hypothesis conditions", *Neuroimage*, vol. 5, pp. 199–212, 1997.

[7] K. J. Friston, P. Jezzard, and R. Turner, "The analysis of functional MRI time-series", *Human Brain Mapping*, vol. 1, pp. 153–171, 1994.

[8] K. J. Friston, A. P. Holmes, J-B. Poline, S. C. R. Williams, R. S. J. Frackowiak, and R. Turner, "Analysis of fMRI time-series revisited", *Neuroimage*, vol. 2, pp. 173–181, 1995.

[9] K. J. Friston, S. Williams, R. Howard, R. S. J. Frackowiak, and R. Turner, "Movement related effects in fMRI time series", *Magn. Res. Med.*, vol. 35, pp. 346–355, 1996.

[10] K. J. Worsley and K. J. Friston, "Analysis of fMRI time-series revisited - again", *Neuroimage*, vol. 2, pp. 173–181, 1995.

[11] S. Thesen, O. Heid, E. Mueller, and L. R. Schad, "Prospective acquisition correction for head motion with image-based tracking for real-time fMRI", *Magn. Res. Med.*, vol. 44, pp. 457–465, 2000.

[12] C. C. Lee, R. C. Grimm, A. Manduca, J. P. Felmlee, R. L. Ehman, S. J. Riederer, and C. R. Jack, "A prospective approach to correct for interimage head rotation in fMRI", *Magn. Res. Med.*, vol. 39, pp. 234–243, 1998.

[13] H. A. Ward, S. J. Riederer, and R. C. Grimm et al., "Prospective multiaxial motion correction for fMRI", *Magn. Res. Med.*, vol. 43, pp. 459–469, 2000.

[14] B. Kim, J. L. Boes, P. H. Bland, T. L. Chenevert, and C. R. Meyer, "Motion correction in fMRI via registration of individual slices into an anatomical volume", *Magn. Res. Med.*, vol. 41, pp. 964–972, 1999.

[15] S. Grootoonk, C. Hutton, J. Ashburner, A. M. Howseman, O. Josephs, G. Rees, K. J. Friston, and R. Turner, "Characterization and correction of interpolation effects in the realignment of fMRI time series", *Neuroimage*, vol. 11, pp. 49–57, 2000.

[16] W.S. Hinshaw and A.H. Lent, "An introduction to NMR imaging: From the Bloch equation to the imaging equation", *Proc. IEEE*, vol. 71, pp. 338–350, 1983.

[17] A. B. Hargreaves, S. S. Vasanawala, M. J. Pauly, and G. D. Nishimura, "Characterization and reduction of the transient response in steady-state MR imaging", *Magn. Res. Med.*, vol. 46, pp. 149–158, 2001.

[18] D. C. Look and D. R. Locker, "Time saving in measurement of NMR and EPR relaxation times", *The Review of Scientific Instruments*, vol. 41, pp. 250–251, 1970.

[19] D. L. Collins, A. P. Zijdenbos, V. Kollokian, J. G. Sled, N. J. Kabani, C. J. Holmes, and A. C. Evans, "Design and construction of a realistic digital brain phantom", *IEEE Trans. Med. Imaging*, vol. 17, pp. 463–468, June 1998.

[20] R. Kwan, A. C. Evans, and G. B. Pike, "An extensible MRI simulator for post-processing evaluation", in *Proceedings of the 4th International Conference on Visualization in Biomedical Computing, VBC '96, Hamburg*, pp. 135–140, September 1996.

[21] M. D. Mitchell, H. L. Kundel, L. Axel, and P. M. Joseph, "Agarose as a tissue equivalent phantom material for nmr imaging", *Magn. Res. Imag.*, vol. 4, pp. 263–266, 1986.

[22] E. T. Bullmore, M. J. Brammer, S. C. R. Williams, S. Rabe-Hesketh, N. Janot, A. David, J. Mellers, R. Howard, and P. Sham, "Statistical methods of estimation and inference for functional MR image analysis", *Magn. Res. Med.*, vol. 35, pp. 261–277, 1996.

Lucian Muresan received his M.Sc. (1994) in Theoretical Physics from the University of Bucharest, Romania. From 1994-1995 he was Research Assistant at the Institute of Physical Chemistry, Romanian Academy, Bucharest, and from 1995-1998 he was Scientific Researcher at the Joint Institute of Nuclear Research, Dubna, Russia. He is currently a Ph.D. candidate at the Institute for Mathematics and Computing Science, University of Groningen, The Netherlands. His research interests include magnetic resonance imaging, computer vision, and software development.

Remco Renken received his M.Sc. (1998) in biophysical chemistry from the University of Groningen, The Netherlands. In 1998 he worked as a researcher for four months at Yale University, New Haven (Connecticut). He received his Ph.D. degree (2004) at the Faculty of Mathematics and Natural Sciences, University of Groningen, The Netherlands. His research interests include functional magnetic resonance imaging, image reconstruction and analysis, and auditory psychophysics.

Jos B. T. M. Roerdink received his M. Sc. ('79) in theoretical physics from the University of Nijmegen, the Netherlands. Following his Ph. D. ('83) from the University of Utrecht and a two-year position ('83-'85) as a Postdoctoral Fellow at the University of California, San Diego, both in the area of stochastic processes, he joined the Centre for Mathematics and Computer Science in Amsterdam. There he worked from 1986-1992 on image processing and tomographic reconstruction. He is currently associate professor of computing science at the University of Groningen, the Netherlands. His current research interests include mathematical morphology, wavelets, biomedical image processing and scientific visualization.

Hendrikus (Diek) Duifhuis received his M. Sc. ('69) in applied physics from the Eindhoven University of Technology (EUT). After his Ph.D. study 'Perceptual Analysis of Sound' at the same university ('72) he spent a postdoctoral year ('72-'73) at the MIT Communications Biophysics Group. He worked in the IPO speech and hearing group (EUT) until 1980, when he was appointed full professor of biophysics at the Department of Physics and Applied Physics of the University of Groningen (RUG). He was one of the initiators of the graduate school of Behavioral and Cognitive Neurosciences (scientific director '89-'98) and is currently responsible for the master programs in physics and applied physics, and in biomedical engineering at the RUG. Current research interests: auditory processing, speech recognition, imaging technology in particular in relation to auditory perception.